PAPER

Adaptive thermal camouflage using sub-wavelength phase-change metasurfaces

To cite this article: Zahra RahimianOmam *et al* 2023 *J. Phys. D: Appl. Phys.* **56** 025104

IOP Publishing Journal of Physics D: Applied Physics
J. Phys. D: Appl. Phys. **56** (2023) 025104 (8pp) https://doi.org/10.1088/1361-6463/aca41d

Adaptive thermal camouflage using sub-wavelength phase-change metasurfaces

Zahra RahimianOmam[1], Amir Ghobadi[1,2,*], Bahram Khalichi[1,2] and Ekmel Ozbay[1,2,3,4,*]

[1] NANOTAM-Nanotechnology Research Center, Bilkent University, 06800 Ankara, Turkey
[2] Department of Electrical and Electronics Engineering, Bilkent University, 06800 Ankara, Turkey
[3] Department of Physics, Bilkent University, 06800 Ankara, Turkey
[4] UNAM-Institute of Materials Science and Nanotechnology, Bilkent University, Ankara, Turkey

E-mail: amir.ghobadi.ee@gmail.com and ozbay@bilkent.edu.tr

Received 2 August 2022, revised 8 November 2022
Accepted for publication 18 November 2022
Published 9 December 2022

Abstract

Sub-wavelength metasurface designs can be used to artificially engineer the spectral thermal signature of an object. The real-time control of this emission can provide the opportunity to switch between radiative cooling (RC) and thermal camouflage functionalities. This performance could be achieved by using phase-change materials (PCMs). This paper presents a sub-wavelength dynamic metasurface design with the adaptive property. The proposed metasurface is made of vanadium dioxide (VO_2) nanogratings on a silver (Ag) substrate. The design geometries are optimized in a way that both narrowband and broadband mid-infrared (MIR) emitters can be realized. At low temperatures, insulating VO_2 nanogratings trigger the excitation of Fabry–Perot mode inside the grating and surface plasmon polaritons at the metal–dielectric interface with an emission peak located in the MIR region to maximize the RC performance of the design. As temperature rises, the PCM transforms into a metallic phase material and supports excitation of Wood's anomaly and localized surface plasmon resonance modes. Accordingly, the thermal signature is adaptively suppressed.

Keywords: thermal camouflage, metasurface, phase-change materials, surface plasmon polaritons, Wood's anomaly resonance

(Some figures may appear in colour only in the online journal)

1. Introduction

In nature, self-adaptions are a defensive strategy used by creatures to conceal their appearance and fit in with their surroundings. Camouflage, also known as cryptic coloring, is the name of this act to conceal the location, identity, and movement. While visual camouflage occurs in the visible regime, the blackbody (BB) radiation in the infrared region is a secondary way to identify and track an object. Thermal camouflage (TC), an ability to suppress or manipulate the emission from a surface, is the common contour measure to hide from thermal cameras' eyes [1, 2]. Two common approaches are described in the literature for controlling the radiant intensity of objects to realize TC. The first one is based on controlling the surface temperature or their surrounding environment [3, 4], while the second approach is based on modifying the surface emissivity of objects by using special material [5–8] and sub-wavelength metasurface designs [9–15]. Compared with the first approach, which requires supplementary cooling and heating devices, surface emissivity control is a more convenient and robust approach to tailoring the thermal emission. The simplest design to achieve TC is metallic foils with near-zero thermal emissivity values in the infrared region. However, a metallic sheet is a non-selective design that reflects the inside heat radiation and causes thermal imbalance. Therefore, a wise

* Authors to whom any correspondence should be addressed.

design requires a selective thermal emission to cool the design radiatively while keeping the thermal signature at low values. Generally, thermal cameras operate in two regions; the mid-wave infrared (MWIR, 3–5 μm) and the long-wave infrared (LWIR, 8–14 μm), which are atmospheric transmission windows, where photons can propagate with minimal attenuation. That is why thermal cameras operate either in the MWIR or LWIR regions. Moreover, in between, we have a non-transmissive spectral range called non-transmissive infrared region (NTIR) (5–8 μm) [16, 17]. Modifying the inherent surface emissivity of an object by using engineered nanoantennas could place the BB radiation in the NTIR region and suppress the MWIR and LWIR signatures [9–11]. Besides this passive modification, achieving dynamic control is the desired functionality in TC. This could be accomplished using phase-change materials (PCMs) such as samarium nickel oxide ($SmNiO_3$) [18], antimony trisulfide (Sb_2S_3) [19], vanadium dioxide (VO_2) [20–24], germanium antimony telluride (GST) [25], and $Ge_2Sb_2Se_4Te_1$ (GSST) [26]. Among the PCMs materials, VO_2 is a particularly promising candidate for the studies conducted on TC technology. It has a rapid phase change from room temperature to 90 °C and has a phase-transition temperature of 68 °C [20, 21]. While these materials, in the bulk form, have non-resonant/non-selective optical response, their integration with metasurface structures such as metal–insulator–metal (MIM) structures, all metallic structures, and gratings can offer the desired selectivity [21, 27–30]. Therefore, different tunable thermal emitters are proposed by utilizing a multilayer metal–dielectric–metal micro pyramid structure with VO_2 spacers [27], inserting a GST interlayer between the top gold nanodisks and bottom gold layer as an MIM configuration [28, 29], and using an ultrathin VO_2 interlayer embedded within the grating [30]. However, the above-mentioned emitters are multilayer configurations and the cavity-based design sensitivity to the incidence angle makes them ineffective under oblique angle conditions.

Herein, we propose a simple facile route to obtain a PCM-based metasurface nanoantenna emitter to realize tunable control of TC. This performance is realized due to the shift of emission peaks between the neighboring windows as VO_2 temperature varies from 25 °C (insulator phase) to 90 °C (metal phase), causing it to operate with high emission within the NTIR region to actively dissipate heat. When the VO_2 lies in the metal phase, by changing the dimensions of the grating, the optical response of the design can be tuned from a narrowband to a broadband thermal emitter in the NTIR region. Moreover, a possible IR sensor's detectability of the structure is calculated using power calculations over the selected spectra.

2. Design methodology, operation principle, and simulation results

Any object with a temperature above zero Kelvin emits its heat as radiation. On the earth, with its nominal temperature, this radiation is mainly located in the infrared region. In the meantime, the atmosphere has selective transmissive windows (MWIR and LWIR), where photons can propagate with minimal attenuation. That is why thermal cameras operate either in the MWIR or LWIR regions. Moreover, we have a non-transmissive spectral region called NTIR, see figure 1(a). Based on the targeted application, the emission spectra of the design can be engineered accordingly. If the goal is radiative cooling (RC), the MWIR and LWIR ranges are preferred regimes where photons can propagate toward space with minimal capturing in the earth's atmosphere. However, from TC perspective, the emission spectra should be placed in the NTIR range to hide an object from thermal cameras as well as sustain its RC performance. Although objects have inherently non-selective BB emissions, it is possible to manipulate their spectral radiation using nanoantennas such as sub-wavelength metasurfaces. The proposed metasurface in this work is shown in figure 1(b). The unit cell of the emitter consists of a PCM

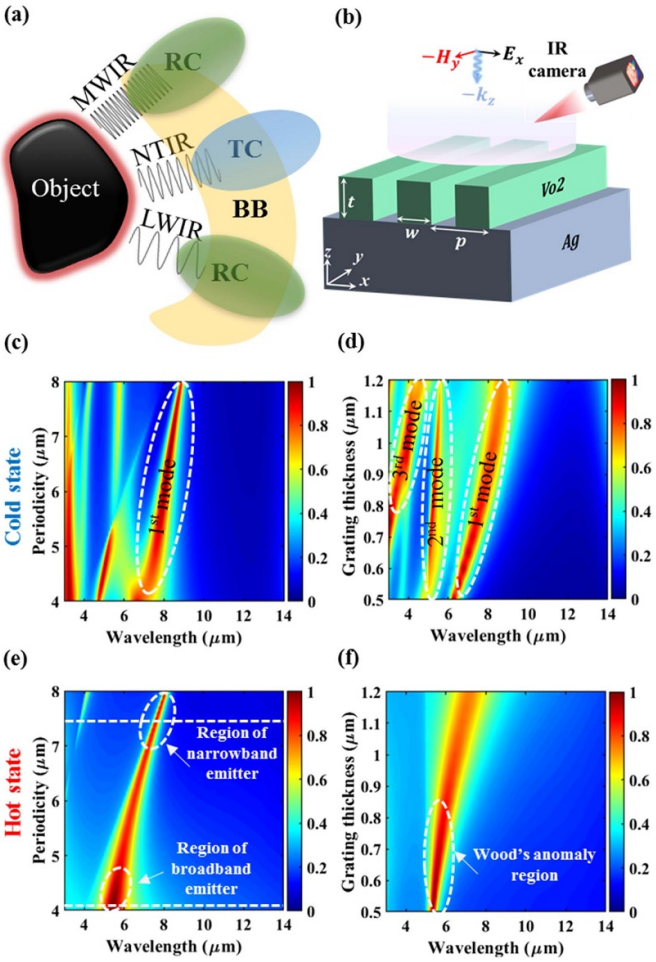

Figure 1. (a) Different detection scenarios of an object. (b) Schematic illustration of the proposed tunable thermal emitter based on phase change material VO_2. The absorption contour plot as a function of wavelength for constant width and thickness of VO_2 grating ($w = 3500$ nm, $t = 800$ nm) versus periodicity for the (c) cold state and (e) hot state. The absorption contour plot as a function of wavelength for constant width and period ($w = 3500$ nm, $p = 5000$ nm) versus thickness of nanograting for the (d) cold state and (f) hot state.

nanograting antenna made of VO_2 on top of a thick silver (Ag) substrate.

The electromagnetic characteristics of the proposed emitter are achieved through a finite difference time domain-based software package. These simulations are carried out in a two-dimensional (2D) environment, and the structure is normally illuminated by an $x-$polarized uniform plane wave propagating along the $-z$ direction. The boundary conditions for the x and z directions are periodic (to calculate the coupling effect between the neighboring meta-atoms) and perfectly matched layers (to evaluate absorptivity). In the simulations, the spectral refractive index of VO_2 grating is extracted from [20], and the Ag substrate is taken from the Johnson and Christy database [31].

The absorption/emission response of the design is numerically evaluated at two extreme states, cold (25 °C) and hot (90 °C). Essentially, the optical response of the proposed metasurface can be manipulated by two main factors; (a) the filling fraction (w/p) and (b) the thickness (t) of the grating. To evaluate these factors, the absorption contour plots (in both cold and hot states) are extracted for periodicity and thickness sweeps under normal illumination of the TM-polarized plane wave, see figures 1(c)–(f). In the cold state, the absorption response has three main resonance modes. The first and third modes have less dependency on periodicity but linearly redshift as the thickness of the grating increases. Contrarily, the spectral position of the second mode is independent of the grating thickness and gradually increases with the periodicity of the design. Moreover, this resonance could only be excited in specific periodicity values ranging below 5.5 μm. When it comes to the hot state, as these panels imply (figures 1(e) and (f)), the response is a single-mode resonator with its peak located within the NTIR region. Based on the choice of p and t, this emitter could be either narrowband or broadband, as shown in figures 1(e) and (f). While the periodicity causes a semi-linear shift in the absorption peak, the thickness effect is more like broadening the peak signal. Thus, upon phase transmission, the operation principle of the nanoantenna emitter significantly changes. The physical mechanisms behind this operation will be discussed later.

To design an adaptive TC nanoemitter, we need to engineer emission response between the atmospheric windows. To suppress the thermal signature of an object upon temperature rise, the emission spectrum of the nanoantenna should shift from the LWIR region to the NTIR region. Taking these criteria as our goal, geometrical optimizations are carried out to design both narrowband and broadband emitters. As shown in figures 2(a) and (b), both emitters have a multi-band absorption response in the cold state. Essentially, in lower temperatures with lower emissive power values, the multi-band response provides an efficient cooling performance through a broad spectral range. However, as the temperature rises, the VO_2 layer undergoes a phase transition, and the emission peak moves toward the NTIR region to suppress the LWIR signature from the object. While the broadband emitter has a better cooling performance, its thermal signature (in the MWIR and LWIR regions) is higher than that of the narrowband one.

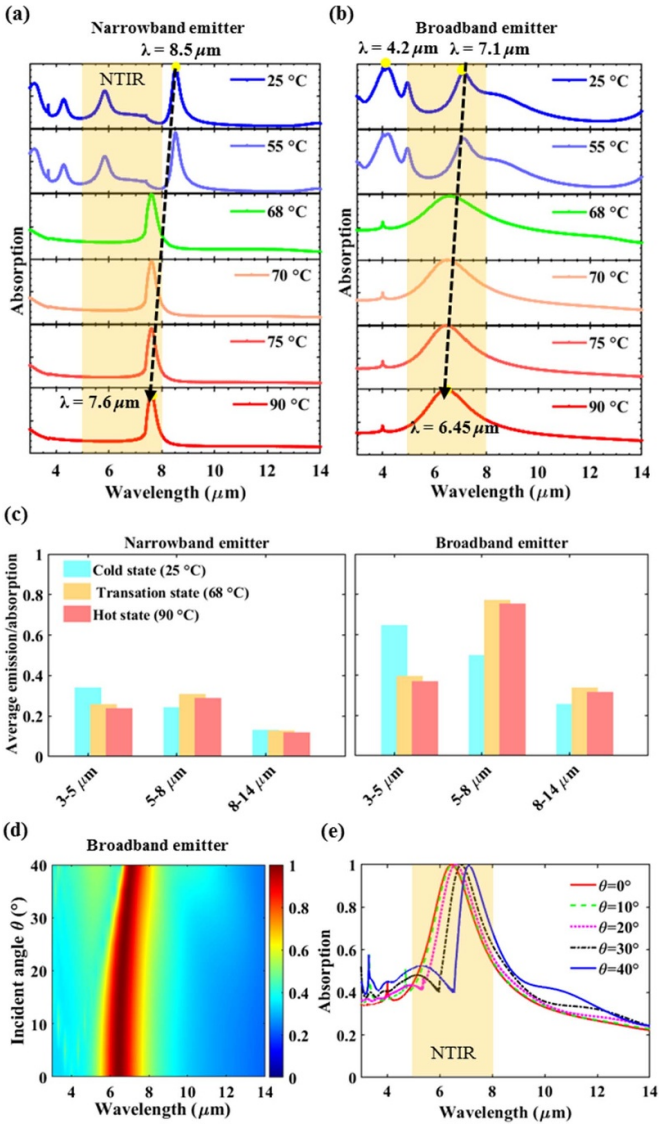

Figure 2. Dependency of the absorption spectrum of the proposed nanoantenna emitter on the variation of the temperature from 25 °C to 90 °C: (a) narrowband emitter ($w = 3800$ nm, $t = 750$ nm, $p = 7400$ nm) and (b) broadband emitter ($w = 3400$ nm, $t = 1050$ nm, $p = 4000$ nm). (c) Calculated average emission/absorption under normal incidence obtained via integration of the absorption spectra with respect to the wavelength at different regions (including MWIR, NTIR, and LWIR regions) for 25 °C, 68 °C, and 90 °C temperatures for the narrowband and broadband emitters. Angular absorption response of the metasurface design for different incident angles (hot state); (d) contour plot and (e) 2D plot.

Thus, the choice of the emitter should consider the trade-off between RC and thermal signature mitigation. For a better qualitative comparison, the average emission/absorption of three distinct states of cold, transition, and hot are extracted in the MWIR, NTIR, and LWIR regions for both narrowband and broadband emitters (figure 2(c)). In the narrowband design, the temperature rise has triggered the suppression of both MWIR and LWIR signatures while maintaining the RC performance. Similar trends can be found in the broadband nanoantenna but with larger amplitudes due to broader spectral response.

Therefore, the proposed metasurface rationally adapts itself to the background temperature through simultaneous thermal signature reduction and NTIR RC enhancement. From a practical point of view, a camouflage design should sustain its operation against threats from all directions. In other words, the metasurface should hold its spectral response at wide viewing angles. For this purpose, the angular absorption response of the metasurface design through an incidence angle range of 0°–40° is investigated. Based on the contour plot depicted in figure 2(d), the absorption peak of the broadband design in the hot state stayed inside the NTIR region within the whole field of view while keeping its MWIR and LWIR signatures almost intact (this effect will be discussed later). This could be visualized from the 2D plot given in figure 2(e). According to the above-mentioned discussions, the proposed metasurface design is an adaptive camouflage structure. However, the question is how it adapts its operation under temperature-variant conditions.

The physical origin of the resonance modes is required to be explored to answer the question. For this aim, the magnetic field (*H*-field) and power absorption density profiles have been extracted along the cross-section of narrowband and broadband designs for both cold and hot states, see figures 3 and 4. The results are investigated for the normal incidence of the transverse magnetic (TM)-polarized wave. The calculated field and absorption density profiles for the narrowband design in the cold (at 8.5 μm) and hot (at 7.6 μm) states are considered in figures 3(a) and (b), respectively. In the cold state (figure 3(a)), the magnetic field is dominantly confined in the grating, demonstrating the formation of a standing wave leading to the excitation of Fabry–Perot (FP) mode. This confinement can also be observed from the absorption density profile, while the main contribution of the absorption is due to the loss inside the dielectric grating. However, in the hot state, the VO_2 grating turns into a lossy metallic layer, forming a metal–metal gating configuration. According to figure 3(b), the *H*-field and absorption density profiles dramatically differ from those provided for the cold state. Unlike the *H*-filed and absorption profiles in the cold state, the field distribution in the hot state is dominantly concentrated at the top region of the grating leading to light absorption around this region. This phenomenon can also be justified by looking at the absorption density profile in the hot state. Considering the metal–metal grating architecture and *H*-field profile, the behavior can be explained based on Wood's anomaly phenomenon. The resonance wavelength of a Wood's anomaly absorber (WAA), experiencing a normal incidence, can be explained as follows [32, 33];

$$\lambda_{\mathrm{res}}^{\mathrm{WA}} = \frac{p}{\sqrt{i^2+j^2}}\sqrt{\frac{\varepsilon_{\mathrm{grating}}}{\varepsilon_{\mathrm{grating}}+1}} \tag{1}$$

where p is the periodicity of the design, i and j are integer values (the grating orders for the reciprocal lattice vectors) and $\varepsilon_{\mathrm{grating}}$ is the permittivity of VO_2 in our case. The formula implies that in a WAA, the resonance wavelength is irrespective of the grating thickness (see figure 1(f) for the region of interest shown by the dashed line in which the grating thickness values are between 500 nm and 800 nm) and width and it is defined by the grating periodicity and permittivity. Therefore, considering the fact that $\varepsilon_{VO_2} \gg 1$, the periodicity is the main factor that defines the resonance wavelength, as can be seen from figure 1(e) for the grating periodicity around 7.4 μm. Therefore, Wood's anomaly phenomenon mainly contributed to the absorption resonance wavelength of the proposed narrowband absorber in the hot state. It should also be noted that Wood's anomaly phenomenon works well when the grating design acts as an isolated nanoantenna (smaller filling factor). In other words, increasing the filling factor diminishes this phenomenon due to the fact that adjacent unit cells cause mutual coupling between nanoantennas, which affects the overall absorption response. Therefore, this effect loses its contribution to the broadband design.

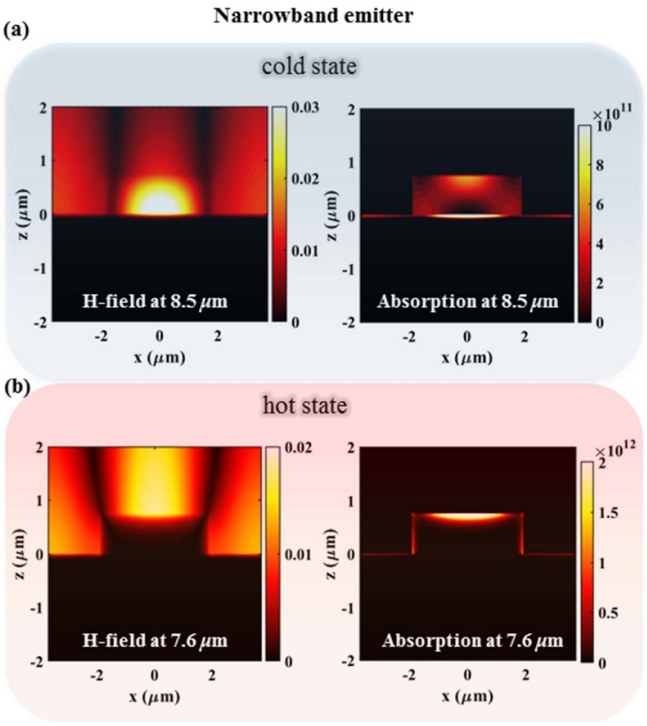

Figure 3. Absolute values of the total magnetic field and power absorption density on the $x-z$ plane obtained for one unit cell at the dominant resonance wavelength of the narrowband design ($w = 3800$ nm, $t = 750$ nm, $p = 7400$ nm) in the (a) cold state and (b) hot state when the structure is normally illuminated by an $x-$polarized uniform plane wave propagating along the $-z$ direction.

In the following, the magnetic field and absorption density profiles have been extracted along the broadband design cross-section for both cold and hot states, see figures 4(a) and (b). Back in figure 2(b), it can be seen that, in the cold state, we have two main resonant peaks located at 4.2 μm and 7.1 μm. The field profile in figure 4(a) demonstrates the formation of a standing wave, leading to the excitation of FP mode. Subsequently, the absorption density profile at 4.2 μm (figure 4(a)) represents light harvesting inside the VO_2 grating, confirming the excitation of FP mode. Moreover, the field distribution at the longer resonance wavelength of 7.1 μm reveals the

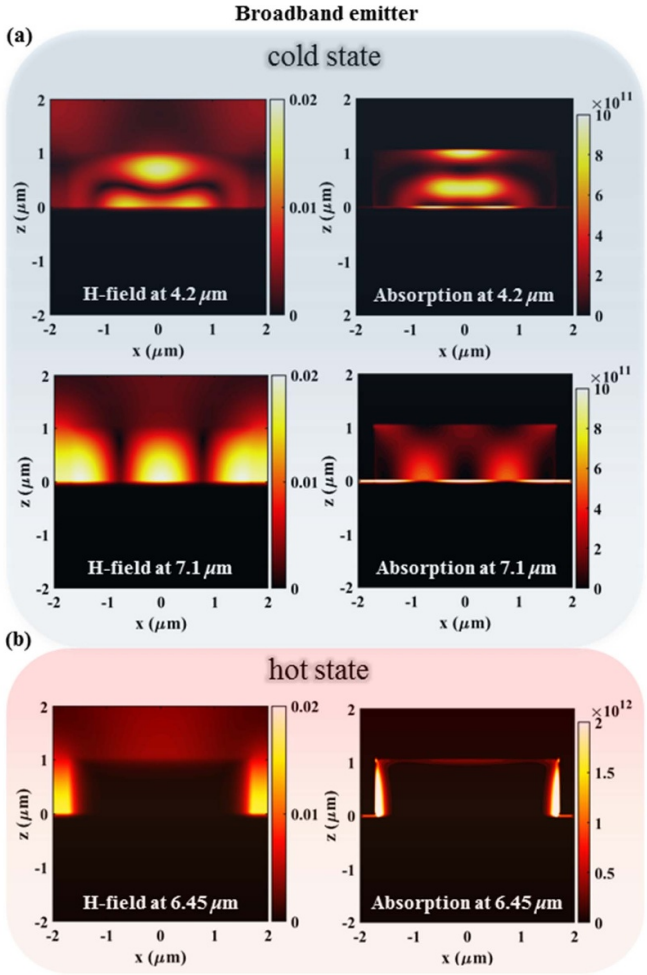

Figure 4. Absolute values of the total magnetic field and power absorption density on the $x-z$ plane obtained for one unit cell at the dominant resonance wavelength of the broadband design ($w = 3400$ nm, $t = 1050$ nm, $p = 4000$ nm) in the (a) cold state and (b) hot state.

excitation of surface plasmon polaritons (SPPs) at the metal–dielectric interface. The absorption density profile given in figure 4(a) reflects the excitation of SPPs at the Ag–VO_2 interface as the main responsible for the light absorption. In particular, surface plasmon resonance wavelength (λ_{res}^{SPP}) excited by a metal–dielectric configuration can be expressed by [34];

$$\lambda_{res}^{SPP} = \mp\frac{p}{m}\sqrt{\frac{\varepsilon_{metal}.n_{eff}^2}{\varepsilon_{metal}+n_{eff}^2}} \tag{2}$$

where p is the periodicity, m is the diffraction order, and n_{eff} is the effective refractive index of the SPP mode (a value between air and grating indices). Considering the IR operation range, it can be assumed that $\varepsilon_{metal} \gg n_{eff}^2$, it simplifies the formula to $\lambda_{res}^{SPP} = \frac{p}{m}n_{eff}$. As a result, the resonance wavelength has a linear relation with the periodicity, which is in line with our findings for the first mode, as explained in figure 1(c). Another factor in defining the resonance wavelength is n_{eff}. While this parameter is directly proportional to the grating width, it can also be manipulated by the grating thickness [35]. This is due to the fact that the SPP fields exponentially decay within the grating region and thickness values, comparable with the SPP decay lengths, can tune the absorption resonance response. Therefore, taking all into consideration, in the cold state, FP and SPP are responsible resonance modes.

In the hot state, the main resonance wavelength is located at 6.45 μm, where the transition of the VO_2 grating results in a metal–metal configuration. In this scenario, as presented in figure 4(b), the magnetic field is mainly concentrated within the groove, leading to the constitution of localized surface plasmons and then light absorption at the grating walls. The corresponding absorption density profile further demonstrates the nature of this resonance as localized surface plasmon resonance mode. This is in contrast to the narrowband design, where Wood's anomaly mainly contributed to the absorption resonance.

Additionally, the design keeps its robustness at a wide viewing angle and the resonance stays inside the NTIR region within the whole field of view as seen in figures 2(d) and (e). In general, the optical path length of the light inside a bulk medium is equal to $k_z\frac{c}{\omega}t$, where k_z represents the z component of the wavevector and t is the layer thickness. In an isotropic medium with a permittivity of ε, $k_z = \frac{\omega}{c}\sqrt{\varepsilon - \sin^2\theta}$, where θ is the incidence angle. In the proposed design, the material is highly dispersive at the resonance wavelength and $\varepsilon \gg \sin^2\theta$. Therefore, the k_z and consequently, the optical path is weakly sensitive to the angle of incidence.

The calculated infrared signatures of the nanoantenna emitter for both narrowband and broadband designs are shown in figure 5. The results are calculated by considering the radiation energy emitted from the normal direction up to 5 km in the cold and hot states of the VO_2 nanograting. The thermal emittance ($\mathrm{TE}(T,\lambda)$) of the nanoantenna emitters over the BB radiator [$\mathrm{TE}(T,\lambda) = \mathrm{BB}(T,\lambda) \times \varepsilon_{emitter}(T,\lambda)$] with and without considering the atmospheric transmission spectrum [$T_{atm}(\lambda) = 1 - \varepsilon_{atmosphere}(\lambda)$] (i.e. $\mathrm{TE}(T,\lambda)$ and $\mathrm{TE}(T,\lambda) \times T_{atm}(\lambda)$) are investigated for each design at both insulating and metallic phases (cold and hot states). From figures 5(a) and (b), it is observed that the IR signatures of the narrowband design (dashed lines) represent a significant reduction in comparison to the BB radiation (light-colored areas) in the atmosphere. While the IR signatures are reduced within the atmospheric windows, the structure can cool itself more efficiently at the range of 5–8 μm, as seen from the solid lines. Compared to the narrowband emitter, it is observed that the broadband design (figures 5(d) and (e)) acts better in RC within the NTIR region but imposes larger MWIR and LWIR signatures. Next, the performance of this metasurface on the average emission of a BB radiator (as an extreme case) is investigated. This is accomplished using the following definition:

$$\varepsilon_{ave}(T) = \frac{\int_{\lambda_1}^{\lambda_2}\mathrm{TE}(T,\lambda)\,\mathrm{d}\lambda}{\int_{\lambda_1}^{\lambda_2}\mathrm{BB}(T,\lambda)\,\mathrm{d}\lambda} = \frac{\int_{\lambda_1}^{\lambda_2}\varepsilon_{emitter}(T,\lambda)\,\mathrm{BB}(T,\lambda)\,\mathrm{d}\lambda}{\int_{\lambda_1}^{\lambda_2}\mathrm{BB}(T,\lambda)\,\mathrm{d}\lambda} \tag{3}$$

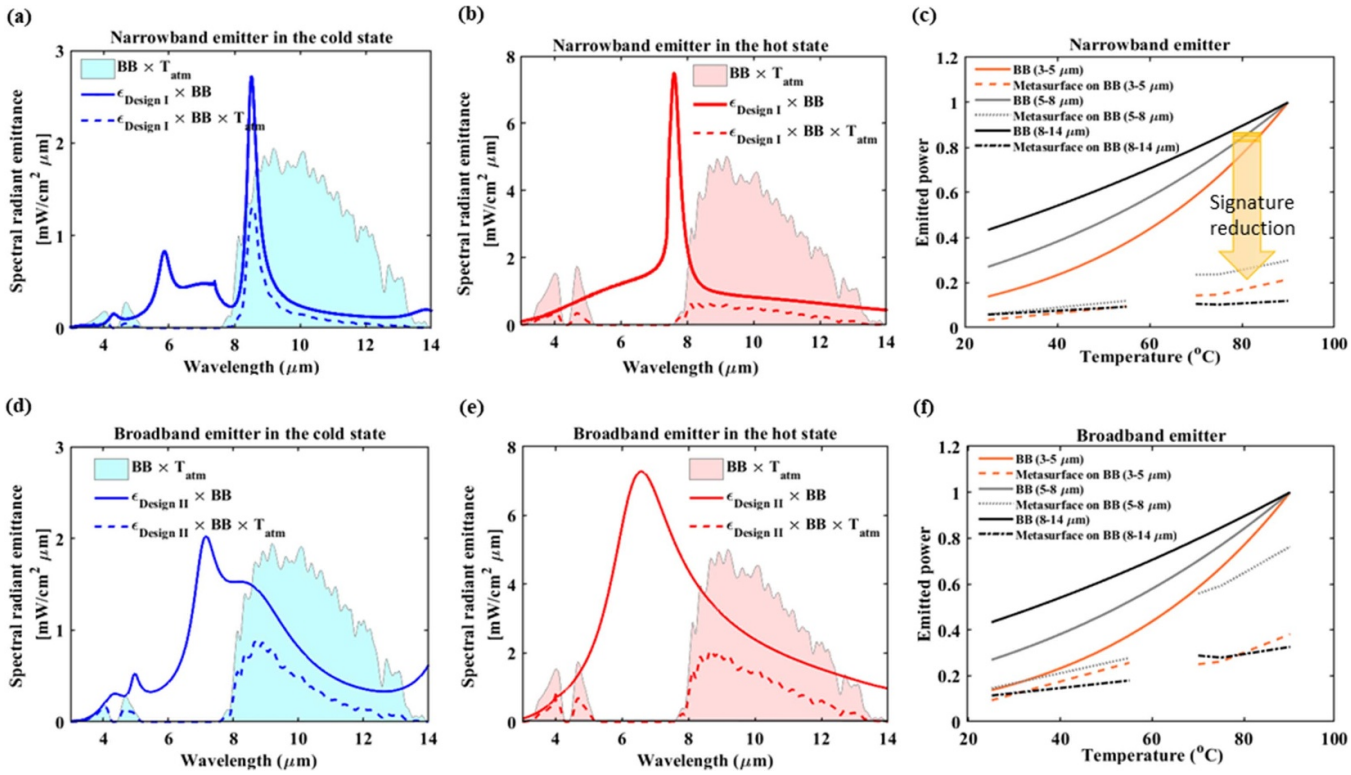

Figure 5. Comparisons among the emitted power densities at different temperatures including BB radiation, atmospheric transmissivity, and the proposed structure response obtained by considering the effect of the atmospheric transmission spectrum. The spectral radiant emittance of (a) the narrowband emitter in the cold state (25 °C) and (b) in the hot state (90 °C) (c) detected emitted power versus temperature at different intervals including 3–5 μm, 5–8 μm, and 8–14 μm for the narrowband design. The spectral radiant emittance of (d) the broadband emitter in the cold state and (e) in the hot state (f) detected emitted power versus temperature at different intervals including 3–5 μm, 5–8 μm, and 8–14 μm for broadband design.

Table 1. Comparisons of proposed PCM-based metasurface nanoantenna emitter and previous published works.

References	Utilized PCM	Structure configuration	Tunability	Sensitivity to the incidence angle
[22]	VO_2	hBN patches and periodic VO_2 blocks on a silicon film	×	×
[26]	GSST	Combining the inner and outer elliptical cylinders	×	×
[27]	VO_2	Multilayer micro pyramid structure with VO_2 spacers	✓	0°–60°
[29]	GST	MIM tri-layer	✓	0°–25°
[30]	VO_2	VO_2 interlayer embedded within the grating	✓	×
This work	VO_2	Single layer of VO_2 grating on Substrate	✓	0°–40°

where $\mathrm{BB}(T,\lambda)$ is the BB emission and $\varepsilon_{\mathrm{emitter}}(T,\lambda)$ is the surface emissivity of the proposed metasurface-based nanoantenna emitter. The results obtained via equation (3) for both narrowband and broadband designs are extracted for a temperature range of 25 °C–55 °C and 70 °C–90 °C, as shown in figures 5(c) and (f). For the narrowband design, the normalized emitted power in MWIR, NTIR, and LWIR ranges are almost temperature-independent with a value below 0.3. In the broadband emitter case, the LWIR, NTIR, and MWIR signature suppressions are not as effective as the narrowband design. However, its RC performance is stronger due to its broader spectral response. The discontinuity of the emitted power versus temperature between 55 °C and 70 °C, corresponding to the transition region of VO_2 material with a hysteresis behavior, is due to the fact that the VO_2 material is effectively in a state between dielectric and metallic phases. Therefore, the permittivity data cannot be modeled appropriately where the emitted power analysis within this specific range is skipped. In the end, a comprehensive comparison of the proposed PCM-based metasurface nanoantenna emitter with prior works in terms of structure configuration, tunability, and sensitivity to the incidence angle is investigated in table 1. It is seen that the proposed PCM-based emitter is capable of providing tunable thermal management throughout a wide viewing angle.

3. Conclusions

This paper demonstrates an adaptive metasurface thermal emitter suitable for TC functionality. The design can sustain its camouflage performance throughout a wide viewing angle, making it a facial structure for real applications. The results of this study can serve as a beacon for the design of future

smart coatings that can adapt themselves to surrounding environments without the need for an external control mechanism.

Data availability statement

The data that support the findings of this study are available upon reasonable request from the authors.

Acknowledgments

One of the authors (E. O.) acknowledges partial support from the Turkish Academy of Sciences.

Conflict of interest

The authors declare no conflict of interest.

ORCID iDs

Amir Ghobadi https://orcid.org/0000-0002-8146-0361
Bahram Khalichi https://orcid.org/0000-0002-9465-1044

References

[1] Hong S, Shin S and Chen R 2020 An adaptive and wearable thermal camouflage device *Adv. Funct. Mater.* **30** 1909788
[2] Li M, Liu D, Cheng H, Peng L and Zu M 2020 Manipulating metals for adaptive thermal camouflage *Sci. Adv.* **6** eaba3494
[3] Li Y, Bai X, Yang T, Luo H and Qiu C W 2018 Structured thermal surface for radiative camouflage *Nat. Commun.* **9** 273
[4] Han T, Bai X, Thong J T L, Li B and Qiu C W 2014 Full control and manipulation of heat signatures: cloaking, camouflage and thermal metamaterials *Adv. Mater.* **26** 1731–4
[5] Lim T, Jeong S M, Seo K, Pak J H, Choi Y K and Ju S 2020 Development of fiber-based active thermal infrared camouflage textile *Appl. Mater. Today* **20** 100624
[6] Mandal J, Du S, Dontigny M, Zaghib K, Yu N and Yang Y 2018 $Li_4Ti_5O_{12}$: a visible-to-infrared broadband electrochromic material for optical and thermal management *Adv. Funct. Mater.* **28** 1802180
[7] Malakoutian M *et al* 2021 Polycrystalline diamond growth on β-Ga_2O_3 for thermal management *Appl. Phys. Express* **14** 055502
[8] Li M, Liu D, Cheng H, Peng L and Zu M 2020 Graphene-based reversible metal electrodeposition for dynamic infrared modulation *J. Mater. Chem.* C **8** 8538–45
[9] Zhu H, Li Q, Zheng C, Hong Y, Xu Z, Wang H, Shen W, Kaur S, Ghosh P and Qiu M 2020 High-temperature infrared camouflage with efficient thermal management *Light Sci. Appl.* **9** 1–8
[10] Qu Y, Li Q, Cai L, Pan M, Ghosh P, Du K and Qiu M 2018 Thermal camouflage based on the phase-changing material GST *Light Sci. Appl.* **7** 1–10
[11] Sun R, Zhou P, Ai W, Liu Y, Li Y, Jiang R, Li W, Weng X, Bi L and Deng L 2019 Broadband switching of mid-infrared atmospheric windows by VO_2-based thermal emitter *Opt. Express* **27** 11537–46
[12] Xiao L *et al* 2015 Fast adaptive thermal camouflage based on flexible VO_2/graphene/CNT thin films *Nano Lett.* **15** 8365–70
[13] Zhao L, Liu H, He Z and Dong S 2018 All-metal frequency-selective absorber/emitter for laser stealth and infrared stealth *Appl. Opt.* **57** 1757–64
[14] Yu H, Zhao Z, Qian Q, Xu J, Gou P, Zou Y, Cao J, Yang L, Qian J and An Z 2017 Metamaterial perfect absorbers with solid and inverse periodic cross structures for optoelectronic applications *Opt. Express* **25** 8288
[15] Khalichi B, Ghobadi A, Osgouei A K, Kocer H and Ozbay E 2021 A transparent all-dielectric multifunctional nanoantenna emitter compatible with thermal infrared and cooling scenarios *IEEE Access* **9** 98590–602
[16] Zhao D, Aili A, Zhai Y, Xu S, Tan G, Yin X and Yang R 2019 Radiative sky cooling: fundamental principles, materials, and applications *Appl. Phys. Rev.* **6** 021306
[17] Lee N, Kim T, Lim J S, Chang I and Cho H H 2019 Metamaterial-selective emitter for maximizing infrared camouflage performance with energy dissipation *ACS Appl. Mater. Interfaces* **11** 21250–7
[18] Shahsafi A *et al* 2019 Temperature-independent thermal radiation *Proc. Natl Acad. Sci. USA* **116** 26402–6
[19] Liu H, Dong W, Wang H, Lu L, Ruan Q, Tan Y S, Simpson R E and Yang J K W 2020 Rewritable color nanoprints in antimony trisulfide films *Sci. Adv.* **6** eabb7171
[20] Kocer H, Cakir M C, Durna Y, Soydan M C, Odabasi O, Isik H, Aydin K and Ozbay E 2021 Exceptional adaptable MWIR thermal emission for ordinary objects covered with thin VO_2 film *J. Quant. Spectrosc. Radiat. Transfer* **262** 107500
[21] Guo Y, Zhang Y, Chai X, Zhang L, Wu L, Cao Y and Song L 2019 Tunable broadband, wide angle and lithography-free absorber in the near-infrared using an ultrathin VO_2 film *Appl. Phys. Express* **12** 071005
[22] Peng C, Ou K, Li G, Zhao Z, Li X, Liu C, Li X, Chen X and Lu W 2021 Tunable and polarization-sensitive perfect absorber with a phase-gradient heterojunction metasurface in the mid-infrared *Opt. Express* **29** 12893
[23] Kalantari Osgouei A, Hajian H, Khalichi B, Serebryannikov A E, Ghobadi A and Ozbay E 2021 Active tuning from narrowband to broadband absorbers using a sub-wavelength VO_2 embedded layer *Plasmonics* **16** 1013–21
[24] Rahimian Omam Z, Ghobadi A, Osgouei A K, Khalichi B and Ozbay E 2022 A fano resonance in dolomite-phase change multilayer design for dynamically tunable omnidirectional monochromatic thermal emission *Opt. Lett.* **47** 5781–4
[25] Guo P, Sarangan A M and Agha I 2019 A review of germanium-antimony-telluride phase change materials for non-volatile memories and optical modulators *Appl. Sci.* **9** 530
[26] Tan J, Zhao Z, Chen R, Feilong Y, Chen J, Wang J, Guanhai L, Xing H, Chen X and Wei L 2022 Polarization-controlled varifocal metalens with a phase change material GSST in mid-infrared *Opt. Express* **30** 32501
[27] Ma W Z, Liu J, Chen W, Chen Y S, Zhuang P P, You X Q, Deng X C, Lin D, Fan Z C and Gu Y 2021 VO_2-based thermally tunable emitter and preliminary design of switching for mid-infrared atmospheric windows *Results Phys.* **31** 105055
[28] Kang Q, Li D, Guo K, Gao J and Guo Z 2021 Tunable thermal camouflage based on GST plasmonic metamaterial *Nanomaterials* **11** 260
[29] Kang Q, Li D, Wang W, Guo K and Guo Z 2022 Multiband tunable thermal camouflage compatible with laser camouflage based on GST plasmonic metamaterial *J. Appl. Phys.* **55** 065103
[30] Buhara E, Ghobadi A, Khalichi B, Kocer H and Ozbay E 2021 Mid-infrared adaptive thermal camouflage using a

phase-change material coupled dielectric nanoantenna *J. Appl. Phys.* **54** 265105
[31] Johnson P B and Christy R W 1972 Optical constants of the noble metals *Phys. Rev.* B **6** 4370–9
[32] Chen C, Wang G, Zhang Z and Zhang K 2018 Dual narrow-band absorber based on metal–insulator–metal configuration for refractive index sensing *Opt. Lett.* **43** 3630–3
[33] Maradudin A A, Simonsen I, Polanco J and Fitzgerald R M 2016 Rayleigh and Wood anomalies in the diffraction of light from a perfectly conducting reflection grating *J. Opt.* **18** 024004
[34] Abutoama M and Abdulhalim I 2017 Angular and intensity modes self-referenced refractive index sensor based on thin dielectric grating combined with thin metal film *IEEE J. Sel. Top. Quantum Electron.* **23** 72–80
[35] He S, Zhang X and He Y 2013 Graphene nano-ribbon waveguides of record-small mode area and ultra-high effective refractive indices for future VLSI *Opt. Express* **21** 30664